








Improving MR axon radius estimation in human white matter using spiral acquisition and field monitoring

Marten Veldmann¹  | Luke J. Edwards²  | Kerrin J. Pine²  | Philipp Ehses¹  |
Mónica Ferreira^{3,4}  | Nikolaus Weiskopf^{2,5,6}  | Tony Stoecker^{1,7} 

¹MR Physics, German Center for Neurodegenerative Diseases (DZNE) e.V., Bonn, Germany

²Department of Neurophysics, Max Planck Institute for Human Cognitive and Brain Sciences, Leipzig, Germany

³Clinical Research, German Center for Neurodegenerative Diseases (DZNE) e.V., Bonn, Germany

⁴University of Bonn, Bonn, Germany

⁵Felix Bloch Institute for Solid State Physics, Faculty of Physics and Earth System Sciences, Leipzig University, Leipzig, Germany

⁶Wellcome Centre for Human Neuroimaging, Institute of Neurology, University College London, London, UK

⁷Department of Physics & Astronomy, University of Bonn, Bonn, Germany

Correspondence

Tony Stoecker, German Center for Neurodegenerative Diseases (DZNE) e.V., MR Physics, Venusberg-Campus 1, Gebäude 99, 53127 Bonn, Germany.
Email: tony.stoecker@dzne.de

Funding information

Seventh Framework Programme, Grant/Award Number: 616905; Bundesministerium für Bildung und Forschung, Grant/Award Number: 01ED2210; Deutsche Forschungsgemeinschaft, Grant/Award Number: 347592254; Horizon 2020 Framework Programme, Grant/Award Number: 681094

Abstract

Purpose: To compare MR axon radius estimation in human white matter using a multiband spiral sequence combined with field monitoring to the current state-of-the-art echo-planar imaging (EPI)-based approach.

Methods: A custom multiband spiral sequence was used for diffusion-weighted imaging at ultra-high *b*-values. Field monitoring and higher order image reconstruction were employed to greatly reduce artifacts in spiral images. Diffusion weighting parameters were chosen to match a state-of-the-art EPI-based axon radius mapping protocol. The spiral approach was compared to the EPI approach by comparing the image signal-to-noise ratio (SNR) and performing a test–retest study to assess the respective variability and repeatability of axon radius mapping. Effective axon radius estimates were compared over white matter voxels and along the left corticospinal tract.

Results: Increased SNR and reduced artifacts in spiral images led to reduced variability in resulting axon radius maps, especially in low-SNR regions. Test–retest variability was reduced by a factor of approximately 1.5 using the spiral approach. Reduced repeatability due to significant bias was found for some subjects in both spiral and EPI approaches, and attributed to scanner instability, pointing to a previously unknown limitation of the state-of-the-art approach.

Conclusion: Combining spiral readouts with field monitoring improved mapping of the effective axon radius compared to the conventional EPI approach.

KEYWORDS

axon radius, EPI, field monitoring, spiral

1 | INTRODUCTION

Axons form the neural pathways in the white matter of the human brain. The axon radius is a crucial factor influencing the speed and efficiency of axonal signal transmission.¹ Previous *ex vivo* studies have associated axonal degeneration with various diseases; for instance, acute axonal damage is a key morphological feature in the early stages of multiple sclerosis.² Therefore, the axon radius could serve as an important biomarker, if accurate noninvasive *in vivo* quantification were possible.

Diffusion-weighted MRI has been proposed as a method for measuring axon radii in the human brain non-invasively.^{3,4} Approaches to model the diffusion-weighted signal in the white matter include both single- and multi-compartment models. Multicompartment models typically differentiate intra-axonal, extra-axonal and free diffusion (CSF) compartments.^{3,5} If any extra-axonal and free water signal is fully suppressed with sufficiently strong diffusion-weighting,⁶ it is possible to reduce the model to only the intra-axonal compartment, where axons are typically modeled as impermeable cylinders with finite axon radius.⁷

Sensitizing the MR signal to the axon radius requires data acquisition with very strong diffusion-weighting, as the signal attenuation due to diffusion perpendicular to the axonal cylinder is typically small. Therefore, high amplitude gradients are required to achieve imaging at high *b*-values. In recent years, the noninvasive quantification of axon radii in the human white matter has come into reach, due to the development of high-performance gradient systems like the Connectom system with gradient strengths of up to 300 mT/m.⁸ However, even with these gradient systems, the sensitivity of the diffusion-weighted signal is still restricted to large axons greater than approximately 3 μm in diameter,⁹ which represent only a small fraction of the axon radius distribution.¹⁰ Additionally, pointwise estimates of axon radii using diffusion MRI are heavily weighted toward the larger radii represented by the tail of the distribution.^{9,11} This makes it difficult to gain any information about the underlying distribution of axon radii within a voxel without making any assumptions regarding that distribution⁴ or further approximations.⁶ In order to maximize the signal attenuation and decrease the resolution limit of axon diameter mapping, the *b*-value has to be maximized while preserving enough signal-to-noise ratio (SNR).

Fast MRI sequences are required to acquire diffusion data at sufficiently short echo times and to achieve reasonable scan times. These sequences typically suffer from artifacts due to magnetic field inhomogeneities and eddy currents. The workhorse of diffusion-weighted MRI is a two-dimensional multi-band single-shot echo-planar

imaging (EPI) sequence¹² used in most diffusion-weighted MRI studies. This sequence offers fast acquisition of the two-dimensional *k*-space, but suffers from susceptibility and eddy current induced geometric distortions. Advanced correction methods in image space have been developed¹³ allowing the elimination of most of these distortion artifacts. Spiral *k*-space trajectories offer a promising alternative to a rectilinear EPI readout, as acquisition starts in the center of *k*-space, resulting in a reduced echo time and potentially higher SNR.¹⁴ However, single-shot spiral acquisitions are prone to artifacts arising from hardware imperfections and eddy currents, especially in the presence of strong diffusion sensitizing gradients. These artifacts typically manifest as image blurring and can not easily be corrected in image space, due to the non-Cartesian acquisition of *k*-space. Measurement of the actual encoding fields during the MR sequence, also termed field monitoring, aims to mitigate these artifacts.¹⁵ Combined with an expanded encoding model, even higher-order eddy current effects can be corrected in the image reconstruction.¹⁶

In this work we used a custom two-dimensional multi-band spiral sequence combined with field monitoring for the quantification of *in vivo* MR axon radius estimates. We compared this approach to an established EPI-based axon radius mapping approach using a protocol, which previously showed high repeatability.¹⁷ SNR measures for both sequences were investigated and the variability of the derived axon radius estimates was compared both within one measurement and across two measurements using a test–retest design.

2 | METHODS

A single-compartment model for the diffusion-weighted signal representing only the intra-axonal space was used to derive axon radius estimates.⁶ Diffusion-weighted images were acquired at two different high *b*-value shells as proposed in Veraart et al.¹⁷ The lower *b*-value was set to 6000 s/mm² to fully suppress the extra-axonal signal, while keeping the sensitivity to the axon radius at a minimum. The higher *b*-value was set to 30 450 s/mm² to maximize the sensitivity to the axon radius, while not exceeding the hardware limits of the scanner and maintaining sufficient SNR.

2.1 | Data acquisition

A multiband single-shot spiral sequence was implemented as part of a pipeline¹⁸ shown in Figure 1. The sequence was created with PyPulseq¹⁹ and exported to the Pulseq file format.²⁰ A spiral *k*-space trajectory with two

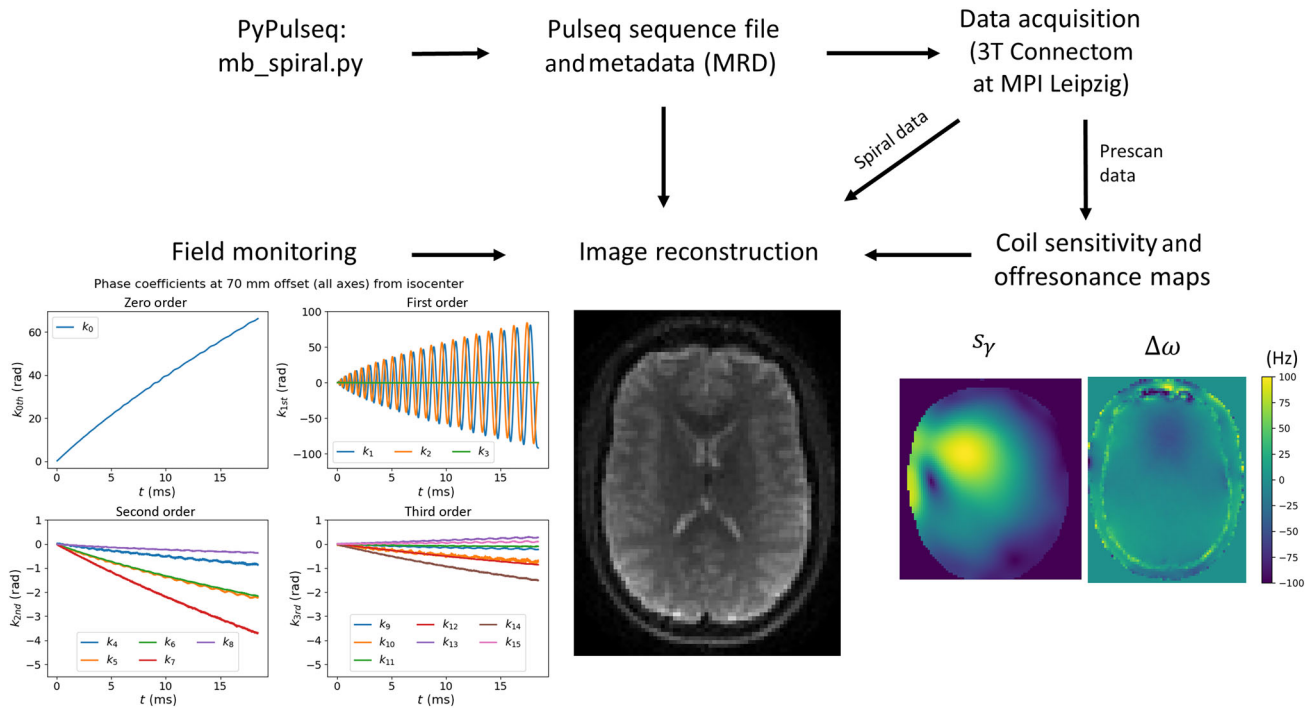


FIGURE 1 Spiral sequence development and image reconstruction pipeline.¹⁸ The spiral sequence was designed using PyPulseq and Pulseq. The sequence includes a dual-echo gradient echo (GRE) prescan for coil sensitivity calibration and mapping of static off-resonance. Image reconstruction with an expanded encoding model was implemented in the PowerGrid toolbox using k-space phase coefficients of up to third spatial order. An example set of phase coefficients measured with a field camera (Skope) is shown on the left.

interleaves was designed for a nominal resolution of 2.5 mm and accelerated by a factor of $R = 2$ by using only the first interleave. The spiral trajectory was implemented with time-optimized gradients.²¹ The sampling dwell time was 2.2 μs with an oversampling factor of two and 8364 samples per shot. The multiband pulses (acceleration factor $MB = 2$) were created from single-band Shinnar–Le Roux radiofrequency (RF) pulses from the vendor’s pulse library, applying a minimum-time VERSE algorithm to reduce peak RF power.²²

The spiral sequence included a dual-echo GRE prescan at $1 \times 1 \times 2.5 \text{ mm}^3$ resolution with an acquisition time of $TA = 1:40 \text{ min}$. Data were acquired at echo times $TE_1 = 2.42 \text{ ms}$ and $TE_2 = 4.84 \text{ ms}$, where the water and fat signals are in phase at a field strength of 3 T. This prescan was used for mapping of the static off-resonance fields and estimation of coil sensitivities. The spiral data were acquired straight axial, with no tilt applied.

A multiband EPI sequence with blipped-CAIPI ($MB = 2$) and in-plane GRAPPA acceleration ($R = 2$)¹² was used as a reference method, as it gave repeatable results in a previous study.¹⁷ In contrast to that study, we only used one instead of two repetitions of the diffusion protocol. The phase-encoding resolution was 88% of the nominal resolution of 2.5 mm, resulting in 77 phase-encoding

lines and 13 552 samples per shot (no partial Fourier). The missing phase-encoding lines were zero-filled in the reconstruction. The EPI sequence uses ramp sampling and the sampling dwell time was 2.5 μs with an oversampling factor of two. The EPI data were acquired with anterior-posterior phase-encoding with a slight tilt along the bottom of the corpus callosum, approximately along the anterior commissure—posterior commissure line.

The following parameters were kept constant for both sequences: $TR = 3.5 \text{ s}$, $FOV = 220 \times 220 \times 135 \text{ mm}^3$, 2.5 mm isotropic voxels. Data were acquired with interleaved b -values $b = 0 \text{ s/mm}^2$ (b_0 ; 10 volumes), $b = 6000 \text{ s/mm}^2$ (60 non-colinear directions on the sphere) and $b = 30450 \text{ s/mm}^2$ (120 non-colinear directions on the sphere) with diffusion gradient parameters $G_{\text{max}} = 280 \text{ mT/m}$ (maximum amplitude), $\Delta = 29.25 \text{ ms}$ (spacing between diffusion gradients) and $\delta = 15 \text{ ms}$ (diffusion gradient duration). For the EPI sequence, 10 b_0 volumes were acquired with inverted phase-encoding direction (posterior-anterior) for susceptibility-induced distortion correction.

The respective echo times of the spiral ($TE = 52 \text{ ms}$) and EPI sequences ($TE = 66 \text{ ms}$) were minimized for the given parameters. The readout durations were 18.4 ms

for the spiral and 22.8 ms for the EPI sequence, and the total acquisition times were $TA = 13:07$ min (spiral) and $TA = 13:27$ min (EPI) including all prescans and the inverted phase-encoding b0 acquisition.

In addition to the diffusion data, T1-weighted anatomical images were acquired with an MPRAGE sequence. These images were used for registration and segmentation of white matter. MPRAGE data were acquired at 1 mm isotropic resolution with a FOV of $256 \times 256 \times 192$ mm³.

Data were acquired from ten healthy volunteers (five male, five female, age between 19 and 36) after giving informed consent on a 3 T Connectom scanner with a maximum gradient strength of 300 mT/m using a 32 channel RF-receive coil (Siemens Healthcare). For each volunteer, test and retest data were collected in two scanning sessions with a short break of 10–20 min in-between using the same imaging protocol. The subject was removed from the scanner and then repositioned during the break. For one subject (subject 7), the test–retest acquisition was repeated twice to investigate the source of a bias in the repeatability metrics observed during the analysis in three of the subjects. The initial scan for this participant had been in the afternoon after several subjects had already been scanned, and so the second acquisition was performed first thing in the morning to investigate the effect of scanner load on the repeatability.

2.2 | Field monitoring and image reconstruction

For the spiral sequence only, the dynamic field evolution was monitored using a field camera (Skopec Magnetic Resonance Technologies AG) with 16 ¹⁹F-based NMR field probes. The spatially-varying field was estimated with spherical harmonic basis functions up to third order and second order concomitant field functions.¹⁵

The field monitoring data were acquired in a separate scan session with the field probes placed inside the RF coil mounted on a plastic frame in optimized positions²³ to allow for third spatial order spherical harmonic fitting. Field data were captured for every second spiral shot as the shot-TR of 130 ms was too low to allow for proper relaxation of the field probes. The field probe data of the missing shots were acquired in a second scan, which was performed after a break to regain the initial state of the MR scanner. The field data collected in this separate scan session was used for reconstruction of spiral data from all subjects.

Image reconstruction was done with an iterative sensitivity encoding (SENSE) reconstruction²⁴ using the PowerGrid toolbox.²⁵ Image reconstruction was based on an expanded signal model¹⁶:

$$\sigma_\gamma(t) = \int \rho(\mathbf{r}) s_\gamma(\mathbf{r}) e^{-i[\sum_j k_j(t) h_j(\mathbf{r}) + \Delta\omega(\mathbf{r})t]} d\mathbf{r} \quad (1)$$

Here, $\sigma_\gamma(t)$ is the signal of receive coil γ at time point t , $\rho(\mathbf{r})$ is the transverse magnetization at voxel position \mathbf{r} and $s_\gamma(\mathbf{r})$ is the sensitivity of the respective receiver coil at that position. The phase term includes the phase coefficients $k_j(t)$, measured with the field camera, multiplied by the respective spatial basis function $h_j(\mathbf{r})$.¹⁵ A zeroth-order phase shift $k_0(t)$ was already applied to the data by the vendor's eddy current compensation (ECC) at the acquisition stage. As the vendor does not allow this ECC to be disabled, this additional global phase shift had to be reversed before image reconstruction. Otherwise, this phase would be corrected twice by the ECC and the field probe data. During conversion of the raw data to the MRD format,²⁶ the global phase $k_0(t)$ applied by the ECC was calculated using the nominal gradient time courses of the sequence and the vendor's eddy current model. Afterwards, the raw data was multiplied by the conjugate of these values to reverse the ECC.¹

The signal model additionally considers the phase evolution due to the spatially dependent static off-resonance field $\Delta\omega(\mathbf{r})$. For the calculation of static off-resonance field maps, phase difference maps between the first and second echo were calculated channel-wise from the GRE prescan using the Hermitian product. After phase-unwrapping, the lowest and highest quartile of phase difference values in a voxel across channels was removed.²⁷ Off-resonance maps were calculated by combining channel-wise maps with a weighted sum, where the weights represent the magnitudes of the respective channels, and dividing by the echo-time difference. Coil sensitivity maps were determined from the first echo of the prescan using the ESPIRiT algorithm.²⁸ The conjugate-gradient algorithm was used to solve the signal model for the image $\rho(\mathbf{r})$.²⁴ Iteration was stopped after a maximum number of 20 iterations or when the relative change of the iteration error norm fell below a threshold of 0.01 %.

2.3 | Image preprocessing

Preprocessing of the images included Gibbs-Ringing correction,²⁹ susceptibility-induced distortion correction, motion correction, eddy current correction up to third order with “FSL eddy”^{13,30,31} and gradient non-linearity correction.³² In the spiral data, “eddy” was only used for motion correction as eddy currents and distortions were already addressed during the reconstruction. The diffusion-weighted images were normalized to the mean non-diffusion-weighted (mean b0) image and spherical-harmonic coefficients of up to sixth

order were calculated for both b -value shells using a maximum-likelihood estimator.³³ In order to account for the Rician distribution of the data, a noise map was calculated³⁴ using only the lower b -value ($b = 6000 \text{ s/mm}^2$) shell and the non-diffusion-weighted images. This noise map was used to improve the precision of the spherical-harmonic fit.

Although, in “eddy” an alignment of the shells is performed, we observed a shift between the two shells in the EPI data after spherical-harmonic fitting. Therefore, in the EPI data an additional registration of the higher b -value shell to the lower b -value shell was done using “FSL FLIRT.”³⁵ The warp fields of “eddy,” the gradient nonlinearity correction and the additional alignment with FLIRT were concatenated to avoid repeated interpolation.

The T1-weighted anatomical images were brain-extracted, denoised and bias field corrected using ANTsPy and ANTsPyNet.³⁶

The exact parameters used in each image (pre)processing step can be found in the Github repository included in the Data Availability Statement.

2.4 | MR axon radius quantification

The powder-averaged signals $\bar{S}(b)$ of both shells were computed from the zeroth-order spherical harmonic coefficients.³⁷ In the absence of extra-axonal signal, the intra-axonal radial diffusivity, D_a^\perp can be estimated from the powder-averaged signals using the relation¹⁷:

$$\bar{S}(b) = \frac{\beta}{\sqrt{b}} e^{-b_{\text{eff}} D_a^\perp}, \quad (2)$$

where β is a signal scaling factor. An effective b -value was calculated for each voxel to account for gradient nonlinearities^{38,39}:

$$b_{\text{eff}} = \frac{1}{n} \sum_{i=1}^n \text{Tr}(\mathbf{B}_{i,\text{eff}}), \quad (3)$$

where n is the number of directions for the respective b -value and \mathbf{B}_{eff} is the effective B-tensor in each voxel. The effective B-tensor was calculated for each direction using the spatial deviations from the nominal magnetic field gradients, which were determined in the gradient nonlinearity correction. The radial diffusivity D_a^\perp was then estimated together with the prefactor β by nonlinear least squares fitting. The MR estimate of the axon radius r_{MR} was calculated with the relation⁶:

$$r_{\text{MR}} = \left(\frac{48}{7} \delta(\Delta - \delta/3) D_0 D_a^\perp \right)^{1/4}, \quad (4)$$

where D_0 is the diffusivity of the axoplasm, which was set to $D_0 = 2500 \mu\text{m}^2/\text{s}$.¹⁷

All axon radius maps were registered to T1-weighted MPRAGE images using FSL FLIRT.³⁵ Afterwards, white matter was segmented based on the T1-weighted images with FSL FAST.⁴⁰ A white matter mask was calculated from white matter partial volume maps using a threshold of > 0.85 . Masks of the corpus callosum were generated using the “Hammersmith n30r95” atlas.⁴¹ The corpus callosum was extracted from the atlas and registered from MNI to T1 space with ANTsPy using the “MNI152-T1 1mm” template. The resulting masks were slightly eroded to avoid including voxels containing CSF.

The axon radius was additionally estimated along the left corticospinal tract (left CST) by applying along-fibre quantification⁴² using Dipy⁴³ and pyAFQ.⁴⁴ In a first step, 3000 tract-specific streamlines were generated for the left CST using MRtrix3.^{45–47} Streamline outliers were removed by a cleaning process described in Reference 42. The ends of the fiber bundle were clipped to a compact bundle without strongly diverging streamlines. Fibre bundles were calculated only once for each subject based on the first spiral dataset after it was registered to the halfway space of the first and second session. Prior to along-fibre quantification, individual datasets were registered to this halfway space.

The bundle was divided into 100 equidistant segments of equal length and the powder-averaged signals of both shells and the effective b -values were averaged in each segment. Gaussian weights were applied in the averaging to suppress contribution from streamlines that diverge strongly from the center line of the bundle.⁴² The axon radius was then estimated for each segment along the tract in the same way as in the voxel-wise analysis.

2.5 | Statistics

SNR measures were generated by dividing the mean b_0 images and the mean images of both shells by the noise map from the denoising step. The ratio of the mean SNR measure between spiral and EPI data in white matter voxels was calculated for all shells across all subjects and both sessions.

In order to investigate the repeatability, the test–retest variability (TRV) of axon radius estimates in the white matter and in segments of the left CST was calculated by¹⁷

$$\text{TRV} = \frac{\sqrt{\pi}}{2N} \sum_{i=1}^N \frac{|\Delta_r(i)|}{\mu_r(i)}, \quad (5)$$

where $\Delta_r(i)$ is the difference and $\mu_r(i)$ the mean axon radius estimate of test and retest for the i th voxel or segment, respectively.

3 | RESULTS

3.1 | SNR comparison

Maps of the SNR measure for the first subject are shown in Figure 2 for the mean images of all shells. The SNR was higher in spiral images compared to EPI in all shells for all white matter regions. The SNR was overall higher in the periphery and in superior parts compared to the center and inferior parts of the brain.

The average SNR gain across all subjects and sessions is shown below the SNR maps as a ratio of spiral and EPI mean SNR values. The SNR gain was higher in the mean b_0 images (30%) and the lower b -value shell (29%) compared to the high b -value shell with 19% SNR gain. The SNR ratio was consistent with a standard deviation of around $\sigma = 0.02$ across all subjects and sessions for all three cases.

3.2 | MR axon radius mapping

Whole-brain maps of the axon radius estimates for the first subject are shown in Figure 3. In the white matter, the axon radius estimates varied mostly between 2 and 3.5 μm . The EPI data showed more voids in the axon radius maps, especially in the frontal lobe and in inferior brain regions, indicating regions where no reasonable axon radius was estimated in the fitting procedure.

Figure 4 shows an overlay of the MR axon radius estimates in the white matter on T1-weighted volumes for the first two subjects. Lower spatial variation of axon radius

estimates across the white matter was observed in the spiral maps compared to EPI maps. Axon radius estimates dropped close to zero especially in inferior regions of the EPI maps, while this was not the case in spiral maps.

The lower variability of axon radius estimates in the spiral data was also reflected in the histograms of these estimates in the white matter (Figure 5), where the SDs were lower for the spiral data in both subjects by around a factor of 1.5. For EPI datasets, the distribution of axon radius estimates had a longer tail toward zero compared to the spiral datasets. Comparing data from all subjects (Figure S1), in almost all cases both the mean and the median of the estimated MR radius were higher in spiral datasets compared to EPI, while the standard deviation was lower in all cases. The histograms in Figure S2 show a direct comparison of spiral and EPI data. The peaks of the axon radius distributions were similar in almost all cases, but the longer tail of EPI distributions led to overall smaller median and mean values. Mean and median values of axon radius estimates in the corpus callosum (Figure S3) differed in some cases from the whole white matter and the standard deviations tended to be slightly higher.

Profiles of the axon radius along segments of the left CST are shown in Figure 6. The mean axon radius estimates across subjects (solid line) were relatively constant across the whole tract in the spiral datasets for both test and retest, while in the EPI datasets, the mean radius increased from inferior towards superior positions. The variability of individual subjects (shaded lines) was also higher in the EPI data compared to spiral data, as indicated by a narrower 95% confidence interval (dashed lines).

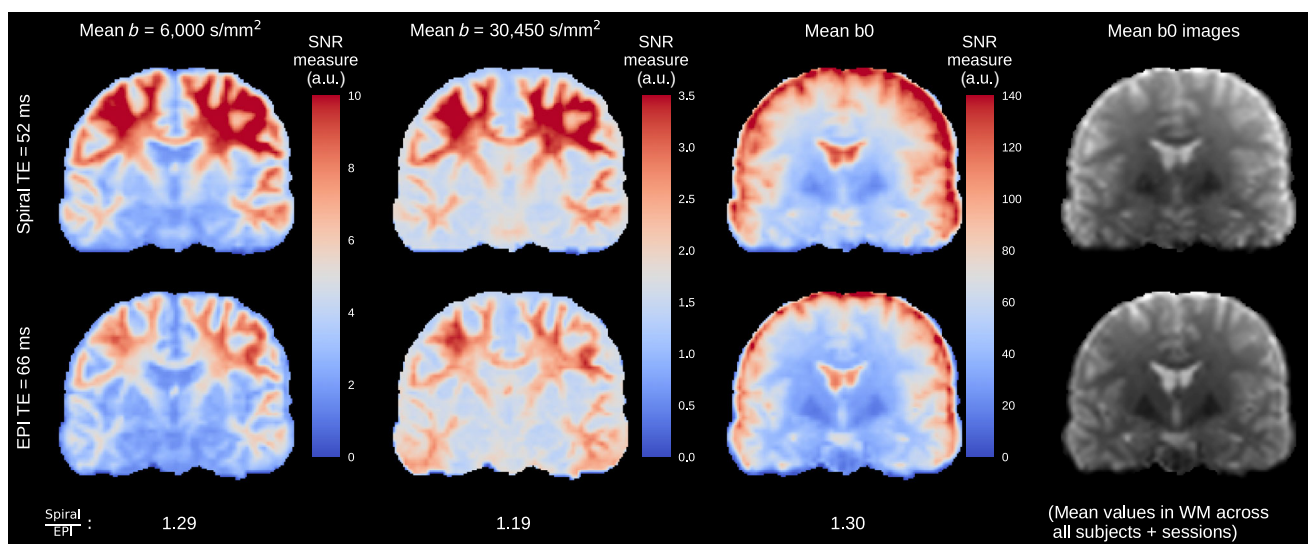


FIGURE 2 Maps of the signal-to-noise ratio (SNR) measure of the first subject for the mean signal of both shells and the mean b_0 signal for spiral (top row) and EPI (bottom row) acquisitions. The last column shows the mean b_0 images. Below the maps, the ratios of the mean SNR measure across all subjects and sessions in the white matter (WM) are displayed.

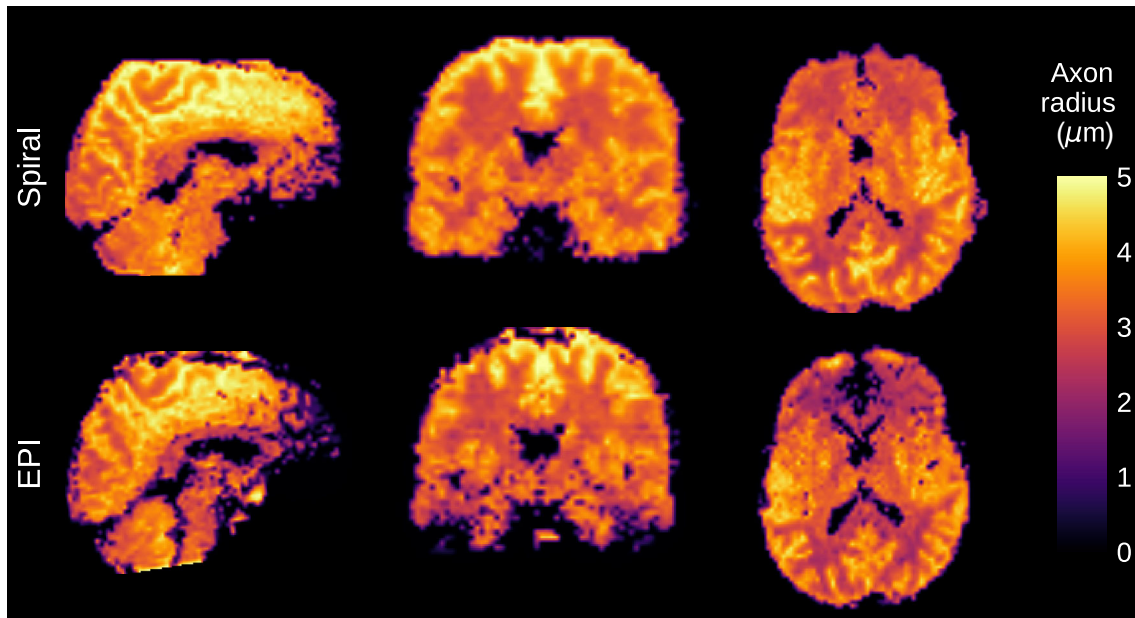


FIGURE 3 Axon radius maps estimated from spiral (top row) and echo-planar imaging (EPI) (bottom row) data of the first subject. The maps are thresholded at $5 \mu\text{m}$, which was the upper bound used in the axon radius fitting procedure.

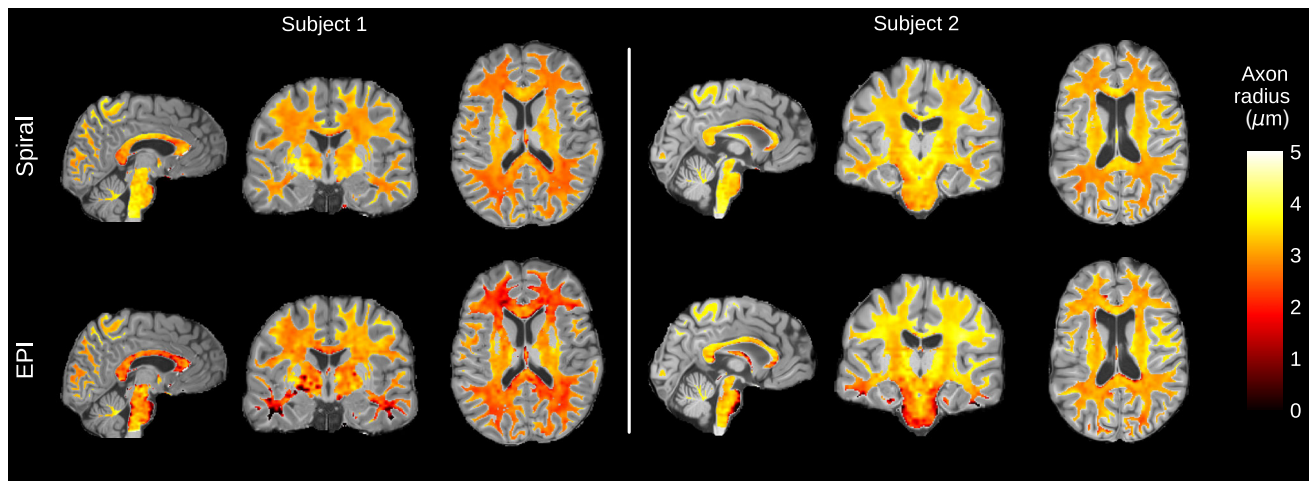


FIGURE 4 Overlay of estimated MR axon radius distributions in the white matter onto anatomical MPRAGE volumes for the first two subjects.

3.3 | Test–retest reliability

The Bland-Altman plots in Figure 7 show the agreement between test and retest measurements. A low absolute mean difference (bias) was observed for most subjects, while for some subjects (e.g., subjects 7 and 10) there was a significant bias of up to 10% of the mean axon radius estimate. In the histograms of MR axon radius estimates in white matter voxels (Figure S1) this bias is observable as a shift in the axon radius distributions. The sign of the bias was consistent across spiral and EPI data, while the absolute amount of bias was similar in most cases.

The variability between test and retest, indicated by the limits of agreement (outer solid lines), was lower by a factor of 1.5–2 in all spiral datasets compared to EPI.

Results for the TRV in the white matter, the corpus callosum and the left CST are shown in Table 1. The TRV in the white matter was approximately 1.5–2 times lower in spiral compared to EPI data. It was relatively consistent across all subjects, except for subjects with a high bias, where the TRV was significantly higher. These observations also hold for the corpus callosum, where however, the TRV was higher compared to the whole white matter. In segments of the left CST, the TRV was lower than

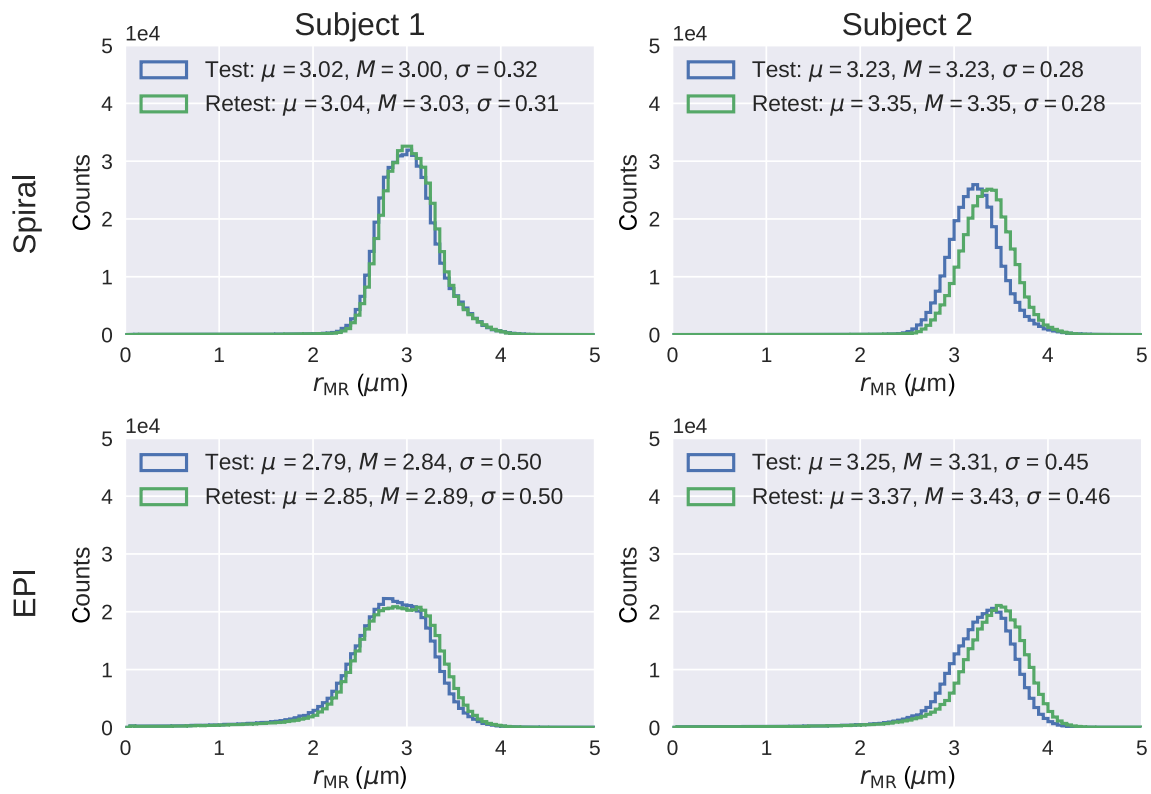


FIGURE 5 Histograms of the MR axon radius (r_{MR}) distributions in white matter of both test and retest measurements for the first two subjects. Mean (μ), median (M), and SD (σ) of the distributions are shown in the legend.

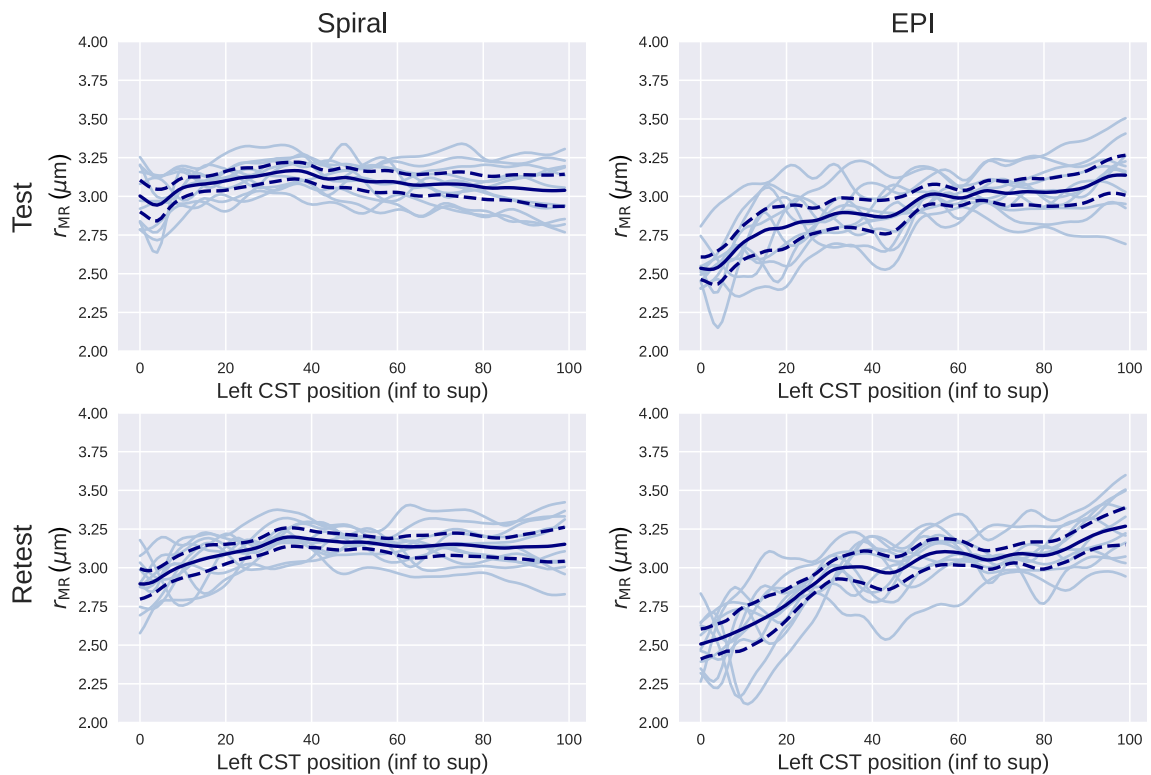


FIGURE 6 Profiles of the estimated axon radius in segments of the left CST from inferior (0) to superior (100) positions. The solid lines represent the mean over all subjects. Dashed lines indicate 95% confidence intervals, calculated as $\pm 1.96 \times \sigma / \sqrt{N}$, where σ is the SD and N the number of subjects. Individual tract profiles are shown as shaded lines.

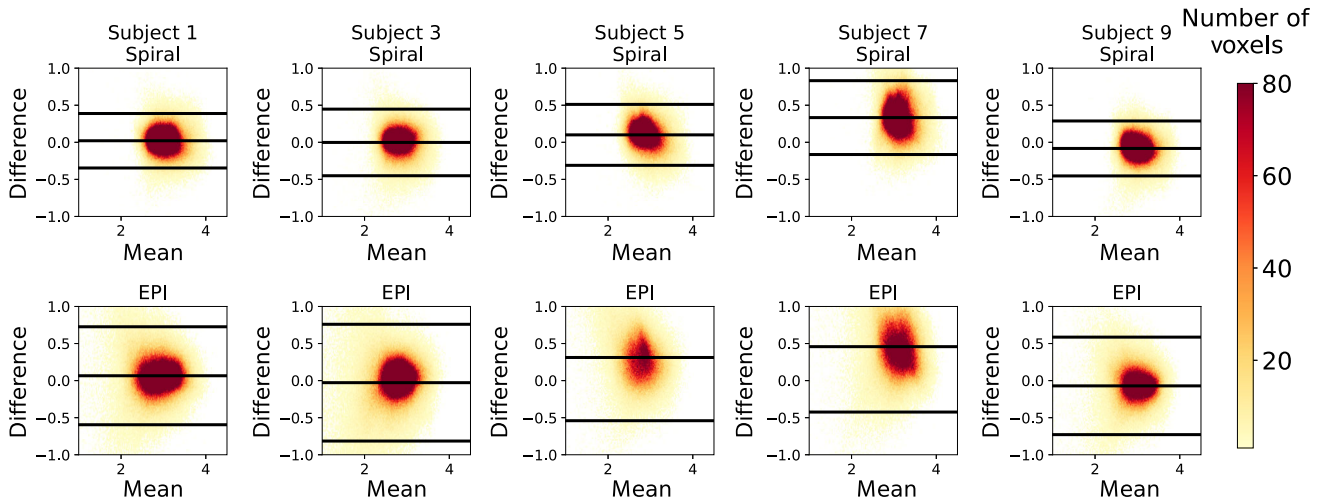


FIGURE 7 Bland–Altman plots of five subjects for all white matter voxels comparing test and retest measurements. Solid lines represent the absolute mean difference and the limits of agreement, calculated as $\pm 1.96 \times \sigma$, where σ is the SD. Bland–Altman plots of all subjects can be found in Figure S4.

TABLE 1 Test–retest variability (TRV; %) in white matter, the corpus callosum (CC) and the left CST of spiral and echo-planar imaging (EPI) datasets.

Subject	1	2	3	4	5	6	7 ^a	8	9	10
WM spiral	4.00	4.48	5.23	4.50	5.65	4.41	10.38/5.34	6.07	4.48	7.77
WM EPI	8.83	6.61	11.72	12.00	15.92	9.74	17.67/7.72	9.72	8.92	13.60
CC spiral	6.06	5.92	9.79	5.88	7.06	6.03	11.98/8.22	5.93	7.31	10.87
CC EPI	14.50	8.70	21.62	12.43	22.39	14.93	23.04/12.11	10.77	14.52	13.41
CST spiral	1.89	2.16	2.66	2.43	4.71	2.55	4.62/2.72	2.12	3.11	4.04
CST EPI	2.82	3.64	3.74	4.77	6.48	2.05	6.74/3.38	3.32	4.52	4.67

Notes: The TRV values in white matter voxels obtained for echo-planar imaging (EPI) data agree with previously reported values, while the TRV in the left CST was slightly higher than in Reference 17.

^aThe test–retest measurement for subject 7 was repeated to investigate the low repeatability in the first measurement.

for the white matter in all cases and lower for spiral data compared to EPI except for subject 6.

Figure 8 shows Bland–Altman plots of both repetitions of the test–retest study for subject 7, who was re-scanned to investigate the high bias in the first test–retest measurement. Variability, bias and TRV (Table 1) were significantly reduced for both spiral and EPI data in the repeated measurement.

4 | DISCUSSION

The results presented in the previous section show, that the spiral acquisition leads to more repeatable results compared to the state-of-the-art EPI-based approach. Reduced variability across the brain is observed in both white

matter voxels and streamlines along the left CST. This is mainly attributed to the higher SNR due to the lower TE of the spiral readout and reduced artifacts by using field monitoring.

The theoretical SNR gain of the spiral acquisition due to shorter TE and therefore reduced T_2 decay would be around 20%, assuming an intra-axonal $T_2 = 75$ ms.^{48,49} This value was exceeded for both the mean b_0 images and the low b -value shell ($b = 6000$ s/mm²). The reduced SNR improvement observed in the high b -value data ($b = 30450$ s/mm²) compared to the lower b -value data could be a result of a suboptimal image reconstruction of the spiral data. The conjugate-gradient method with least squares regularization adds noise to the reconstructed images at each iteration step. It is therefore important to find the optimal stopping point especially under low-SNR

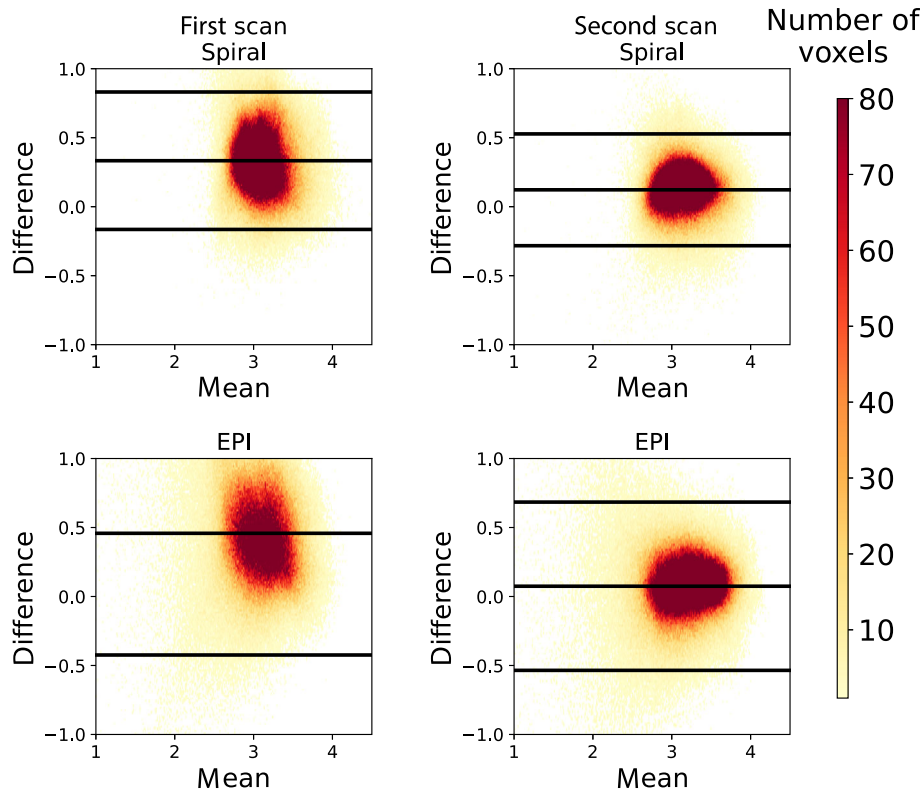


FIGURE 8 Bland–Altman plot of subject 7. The test–retest study for this subject was repeated in a second scan to investigate the large bias in the first scan.

conditions.⁵⁰ SNR might additionally be affected by the 20% lower readout time of the spirals compared to the EPI readout. Although it is possible to increase the readout time of the spirals, that would result in increased susceptibility-induced artifacts such as blurring. Partial volume effects can be ruled out as a cause of the higher SNR ratio in the mean b_0 and lower b -value shell, as similar SNR ratios were observed using a tighter white matter mask (Table S1).

Spiral and EPI trajectories were designed for the same nominal resolution, but are affected differently by T_2^* decay. The effective resolution is reduced by T_2^* blurring, which has a stronger effect on spirals as outer k -space is acquired later than in EPI.¹⁴ In this study, this is partly compensated by the reduced nominal resolution of the EPI sequence in the phase-encoding direction. Matching the effective resolution would require increasing the nominal resolution of the spirals and therefore a longer readout, resulting in a smaller voxel size and therefore decreased SNR.

EPI-based axon radius maps showed more artifacts compared to spiral data, which we mainly attribute to lower SNR and insufficient correction of eddy currents. The eddy current correction with the image-based data-driven approach in “eddy” is limited in the presence of strong diffusion gradients, where low SNR makes registration of diffusion volumes challenging and higher

order eddy currents become more significant. The direct measurement of higher order fields leads to improved correction of eddy current-induced artifacts.^{51,52} Insufficient correction of eddy currents results in local distortions of the images. The amount of distortion varies with different b -values and diffusion gradient directions. We observed submillimeter spatial shifts between the two shells in powder-averaged images, resulting in voids in the axon radius maps. Less distortion and a higher SNR in spiral images led to lower spatial variation in the estimation of the axon radius. This is especially observable in inferior regions of the brain, where the SNR is lower and the axon radius from EPI data is underestimated compared to that from spiral data. Existing comparisons in the literature between EPI with and without field monitoring,⁵³ as well as EPI and spiral readouts^{14,54} have shown that while using field monitoring for EPI data does reduce geometric distortions and ghosting, the spiral data shows higher SNR.

Mean axon radius estimates in the white matter (Figure S1) tended to be higher than previously published results both in the whole white matter and the corpus callosum.^{17,55} Axon radius estimates from spiral data were also on average higher compared to EPI. Two possible confounding factors could have led to these results. First, the Gaussian noise is estimated from strongly diffusion-weighted images with relatively low SNR, which

leads to an underestimation of the noise level.⁵⁶ This may have resulted in an insufficient correction of Rician bias during spherical averaging. Insufficient bias correction leads to an overestimation of the spherically-averaged signal of the high b -value shell and consequently to lower estimates of the axon radius. This effect is stronger in EPI images, as they have lower SNR. Acquisition of additional data at lower b -value as in Reference 17 solely used for noise mapping could improve noise estimation, as potential Rician bias in the noise map would be avoided, but also increase scan time. We found only small differences when estimating axon radii from the data acquired in Reference 17 with noise maps based on lower and higher b -value data, though. The second confounding factor could be insufficient decay of the extra-axonal signal in spiral images due to the lower TE compared to EPI. This effect would lead to an overestimation of the spherically averaged signal in the lower b -value shell and therefore to higher radius estimates.

Along-tract profiles of the axon radius estimates in the left CST showed lower variability between subjects in the spiral data. The TRV was lower for spiral data compared to EPI, in agreement with the results in the white matter. The EPI data showed a decreasing trend toward inferior regions, which could be caused by the low SNR in this region. The decreasing trend toward superior regions reported in a previous study¹⁷ was not observed in the data. Instead, we observed a decreasing trend towards inferior positions in the EPI data, which we relate to low SNR and artifacts in inferior areas in the EPI data. A possible confounding factor could be the difference in b -value along the tract due to gradient nonlinearities (Figure S5). A lower b -value at the edges of the tracts could have an impact on the suppression of the extra-axonal compartment. However, the observed difference of the b -value along the tract of less than 3% was relatively small and did not match the pattern of the along-tract profiles.

The test–retest study showed a lower variability in axon radius maps based on spiral data compared to EPI. TRV values were significantly lower for spiral data in white matter voxels, the corpus callosum and the segments along the left CST. The TRV values obtained for the EPI data in white matter agreed with previously reported values, while the TRV in the left CST tended to be slightly higher.¹⁷ The study in Reference 17 averaged over two repetitions, while we only acquired one repetition, which could explain the higher TRV.

The lower TRV in white matter of spirals (mean TRV including the repeated participant: 5.66%) compared to EPI (mean TRV: 11.13%) results in smaller sample sizes needed to distinguish between cohorts. An example power analysis (significance level $\alpha = 5\%$, power $1 - \beta = 0.95$)

assuming a percentage difference in axon radius estimates of 10% (effect size spiral/EPI: 1.77/0.90) yields sample sizes of 8 (spiral) and 28 (EPI) samples per group (one-sided t -test).^{57,58}

While good repeatability was observed for most subjects, significant bias was apparent in some subjects, indicating a systematic error in the measurement. This bias could potentially arise from the subject, from the data acquisition, or from the image (pre)processing.

Regarding subjects, we found no larger motion in subjects with high bias compared to subjects with low bias. We also observed similar bias in spiral and EPI scans, suggesting a limited impact of subject motion. We found no apparent drift of the diffusion signal intensity during one axon radius measurement (data not shown)⁵⁹ and no relation between the bias and the average SNR over the white matter mask. We also investigated whether the off-isocenter position of the subject could be a cause, as gradient nonlinearities of the Connectom scanner increase strongly with increasing distance to the isocenter.⁶⁰ The absolute distance from the center of the FOV to the isocenter is shown in Table S2 for both test and retest, along with the distance between test and retest positions and the observed bias for each subject. However, no relation between the bias and the absolute off-center position or the difference in position between test and retest was found. Repetition of the acquisition for one of the subjects showing strong bias gave a much smaller bias, suggesting that the bias is not inherent to a given subject.

Regarding image processing, different parameter settings for the eddy current and motion correction procedures were tested, none of them having an impact on the bias. We also tried denoising of complex spiral data³⁴ to reduce the Rician bias before spherical-harmonic calculations, which also did not change the bias. To rule out the possibility that differences in pipeline could cause the bias, the whole image processing pipeline was also tested on a dataset acquired in a previous study,¹⁷ where low bias was reported for all subjects studied. The same low bias was obtained using our own pipeline for that data.

Regarding the acquisition, strong bias was seen in both EPI and spiral when it was seen at all. There also seemed to be a connection between strong bias and multiple subjects scanned in 1 day (but not a connection with just time of day). Together, this suggests that the bias might be due to usage-induced scanner drift. To investigate this, we calculated the percentage difference of the powder-averaged signals between the two sessions for subjects with small, moderate and large bias of the MR axon radius estimates (Figure S6) and found that the bias mainly resided in the high b -value shell. Gradient instabilities might cause such

deviations, as the actual b -value would then differ from the nominal b -value. Therefore, the test–retest study for subject 7 was repeated in the morning without any prior scanning giving improved results. The bias observed in the first test–retest study would be equivalent to a deviation of the high b -value of around 15%, corresponding to a 7.2% or 20 mT/m difference in gradient amplitude. Such strong instabilities of the gradients would typically not be expected, and may reflect as yet unknown limitations of the scanner hardware when it is pushed to its limits over long durations in the course of a day. It is relevant to note that in the study in Reference 17, only one or two participants were recorded in a day, and always in the morning (personal communication from Jelle Veraart), which is in line with our observations.

5 | CONCLUSIONS

Combining spiral k -space trajectories with field monitoring improved axon radius mapping in the white matter compared to a state-of-the-art EPI-based approach. The proposed approach both increased SNR and reduced artifacts in the strongly diffusion-weighted images, leading to reduced variability in resulting maps of the effective axon radius.

While the test–retest repeatability was good in most subjects, limited repeatability due to significant bias was found for some subjects after running the protocol multiple times in a day, suggesting that scanner stability could be an issue. This represents a previously unknown limitation of the axon radius mapping protocol which was independent of the readout method used. However, the precise origin of the observed bias requires further investigation.

FUNDING INFORMATION

This project has received funding from the Federal Ministry of Education and Research (BMBF) under support code 01ED2210. The research leading to these results has received funding from the European Research Council under the European Union's Seventh Framework Programme (FP7/2007-2013)/ERC grant agreement No 616905. NW received funding from the Deutsche Forschungsgemeinschaft (DFG, German Research Foundation)—project number 347592254 (WE 5046/4-2) and from the European Union's Horizon 2020 research and innovation programme under the grant agreement number 681094.

ACKNOWLEDGMENTS

Financial support from the German Chapter of the ISMRM is gratefully acknowledged. The authors also

thank Jelle Veraart for helpful discussions on this topic. We thank Dr Thomas Witzel for providing the two-dimensional-multiband EPI diffusion sequence. The authors thank the ISMRM Reproducible Research Study Group for conducting a code review of the code supplied in the Data Availability Statement. The scope of the code review covered only the code's ease of download, quality of documentation, and ability to run, but did not consider scientific accuracy or code efficiency.

CONFLICTS OF INTEREST STATEMENT

The Max Planck Institute for Human Cognitive and Brain Sciences and Wellcome Centre for Human Neuroimaging have institutional research agreements with Siemens Healthcare. NW holds a patent on acquisition of MRI data during spoiler gradients (US 10,401,453 B2). NW was a speaker at an event organized by Siemens Healthcare and was reimbursed for the travel expenses.

DATA AVAILABILITY STATEMENT

The complete image processing and analysis pipeline, as well as the sequence source code and the Pulseseq sequence file are available in the Github repository <https://github.com/mrphysics-bonn/AxonDiameter> (DOI: 10.5281/zenodo.10797780). A Docker container including the pipeline as well as example datasets are available in the Github repository. The source code of the spiral reconstruction pipeline is available at <https://github.com/mrphysics-bonn/python-ismrmd-reco>.

ENDNOTE

¹https://github.com/SkopeMagneticResonanceTechnologies/siemens_to_ismrmd.

ORCID

Marten Veldmann  <https://orcid.org/0000-0003-2444-9649>

Luke J. Edwards  <https://orcid.org/0000-0002-8320-7298>

Kerrin J. Pine  <https://orcid.org/0000-0002-2486-2970>

Philipp Ehse  <https://orcid.org/0000-0002-5839-6525>

Mónica Ferreira  <https://orcid.org/0009-0007-2844-8850>

Nikolaus Weiskopf  <https://orcid.org/0000-0001-5239-1881>

Tony Stoecker  <https://orcid.org/0000-0002-8946-9141>

REFERENCES

1. Waxman SG. Determinants of conduction velocity in myelinated nerve fibers. *Muscle Nerve*. 1980;3:141-150.
2. Kuhlmann T, Lingfeld G, Bitsch A, Schuchardt J, Brück W. Acute axonal damage in multiple sclerosis is most extensive in early disease stages and decreases over time. *Brain*. 2002;125:2202-2212.

3. Assaf Y, Blumenfeld-Katzir T, Yovel Y, Basser PJ. Axcaliber: a method for measuring axon diameter distribution from diffusion MRI. *Magn Reson Med*. 2008;59:1347-1354.
4. Alexander DC, Hubbard PL, Hall MG, et al. Orientationally invariant indices of axon diameter and density from diffusion MRI. *Neuroimage*. 2010;52:1374-1389.
5. Huang SY, Nummenmaa A, Witzel T, et al. The impact of gradient strength on in vivo diffusion MRI estimates of axon diameter. *Neuroimage*. 2015;106:464-472.
6. Veraart J, Nunes D, Rudrapatna U, et al. Noninvasive quantification of axon radii using diffusion MRI. *Elife*. 2020;9:e49855.
7. Veraart J, Fieremans E, Novikov DS. On the scaling behavior of water diffusion in human brain white matter. *Neuroimage*. 2019;185:379-387.
8. Setsompop K, Kimmlingen R, Eberlein E, et al. Pushing the limits of in vivo diffusion MRI for the human connectome project. *Neuroimage*. 2013;80:220-233.
9. Nilsson M, Lasić S, Drobnjak I, Topgaard D, Westin CF. Resolution limit of cylinder diameter estimation by diffusion MRI: the impact of gradient waveform and orientation dispersion. *NMR Biomed*. 2017;30:e3711.
10. Aboitiz F, Scheibel AB, Fisher RS, Zaidel E. Fiber composition of the human corpus callosum. *Brain Res*. 1992;598:143-153.
11. Burcaw LM, Fieremans E, Novikov DS. Mesoscopic structure of neuronal tracts from time-dependent diffusion. *Neuroimage*. 2015;114:18-37.
12. Setsompop K, Cohen-Adad J, Gagoski BA, et al. Improving diffusion MRI using simultaneous multi-slice Echo planar imaging. *Neuroimage*. 2012;63:569-580.
13. Andersson JLR, Sotiropoulos SN. An integrated approach to correction for off-resonance effects and subject movement in diffusion MR imaging. *Neuroimage*. 2016;125:1063-1078.
14. Lee Y, Wilm BJ, Brunner DO, et al. On the signal-to-noise ratio benefit of spiral Acquisition in Diffusion MRI. *Magn Reson Med*. 2021;85:1924-1937.
15. Barmet C, De Zanche N, Pruessmann KP. Spatiotemporal magnetic field monitoring for MR. *Magn Reson Med*. 2008;60:187-197.
16. Wilm BJ, Barmet C, Pavan M, Pruessmann KP. Higher order reconstruction for MRI in the presence of spatiotemporal field perturbations. *Magn Reson Med*. 2011;65:1690-1701.
17. Veraart J, Raven EP, Edwards LJ, Weiskopf N, Jones DK. The variability of MR axon radii estimates in the human white matter. *Hum Brain Mapp*. 2021;42:2201-2213.
18. Veldmann M, Ehses P, Chow K, Nielsen JF, Zaitsev M, Stöcker T. Open-source MR imaging and reconstruction workflow. *Magn Reson Med*. 2022;88:2395-2407.
19. Ravi KS, Geethanath S, Vaughan J. PyPulseq: a python package for MRI pulse sequence design. *J Open Source Softw*. 2019;4:1725.
20. Layton KJ, Kroboth S, Jia F, et al. Pulseq: a rapid and hardware-independent pulse sequence prototyping framework. *Magn Reson Med*. 2017;77:1544-1552.
21. Lustig M, Kim SJ, Pauly JM. A fast method for designing time-optimal gradient waveforms for arbitrary k-space trajectories. *IEEE Trans Med Imaging*. 2008;27:866-873.
22. Hargreaves BA, Cunningham CH, Nishimura DG, Conolly SM. Variable-rate selective excitation for rapid MRI sequences. *Magn Reson Med*. 2004;52:590-597.
23. Dietrich BE, Brunner DO, Wilm BJ, et al. A field camera for MR sequence monitoring and system analysis. *Magn Reson Med*. 2016;75:1831-1840.
24. Pruessmann KP, Weiger M, Börner P, Boesiger P. Advances in sensitivity encoding with arbitrary K-space trajectories. *Magn Reson Med*. 2001;46:638-651.
25. Cerjanic A, Holtrop JL, Ngo GC, et al. PowerGrid: a open source library for accelerated iterative magnetic resonance image reconstruction. *Proc Intl Soc Mag Res Med*. 2016;24:525.
26. Inati SJ, Naegele JD, Zwart NR, et al. ISMRM raw data format: a proposed standard for MRI raw datasets. *Magn Reson Med*. 2017;77:411-421.
27. Robinson S, Jovicich J. B0 mapping with multi-channel RF coils at high field. *Magn Reson Med*. 2011;66:976-988.
28. Uecker M, Lai P, Murphy MJ, et al. ESPIRiT - an eigenvalue approach to autocalibrating parallel MRI: where SENSE meets GRAPPA. *Magn Reson Med*. 2014;71:990-1001.
29. Kellner E, Dhital B, Kiselev VG, Reiser M. Gibbs-ringing Artifact removal based on local subvoxel-shifts: Gibbs-ringing Artifact removal. *Magn Reson Med*. 2016;76:1574-1581.
30. Andersson JLR, Graham MS, Drobnjak I, Zhang H, Filippini N, Bastiani M. Towards a comprehensive framework for movement and distortion correction of diffusion MR images: within volume movement. *Neuroimage*. 2017;152:450-466.
31. Andersson JLR, Graham MS, Zsoldos E, Sotiropoulos SN. Incorporating outlier detection and replacement into a non-parametric framework for movement and distortion correction of diffusion MR images. *Neuroimage*. 2016;141:556-572.
32. Janke A, Zhao H, Cowin GJ, Galloway GJ, Doddrell DM. Use of spherical harmonic deconvolution methods to compensate for nonlinear gradient effects on MRI images. *Magn Reson Med*. 2004;52:115-122.
33. Sijbers J, Den Dekker AJ, Scheunders P, Van Dyck D. Maximum-likelihood estimation of Rician distribution parameters. *IEEE Trans Med Imaging*. 1998;17:357-361.
34. Cordero-Grande L, Christiaens D, Hutter J, Price AN, Hajnal JV. Complex diffusion-weighted image estimation via matrix recovery under general noise models. *Neuroimage*. 2019;200:391-404.
35. Jenkinson M, Bannister P, Brady M, Smith S. Improved optimization for the robust and accurate linear registration and motion correction of brain images. *Neuroimage*. 2002;17:825-841.
36. Tustison NJ, Cook PA, Holbrook AJ, et al. The ANTsX ecosystem for quantitative biological and medical imaging. *Sci Rep*. 2021;11:9068.
37. Afzali M, Knutsson H, Özarlan E, Jones DK. Computing the orientational-average of diffusion-weighted MRI signals: a comparison of different techniques. *Sci Rep*. 2021;11:14345.
38. Bammer R, Markl M, Barnett A, et al. Analysis and generalized correction of the effect of spatial gradient field distortions in diffusion-weighted imaging. *Magn Reson Med*. 2003;50:560-569.
39. Paquette M, Eichner C, Anwender A. Gradient non-linearity correction for spherical mean diffusion imaging. *Proc Int Soc Mag Reson Med*. 2019;27:550.
40. Zhang Y, Brady M, Smith S. Segmentation of brain MR images through a hidden Markov random field model and the expectation-maximization algorithm. *IEEE Trans Med Imaging*. 2001;20:45-57.

41. Hammers A, Allom R, Koeppe MJ, et al. Three-dimensional maximum probability atlas of the human brain, with particular reference to the temporal lobe. *Hum Brain Mapp.* 2003;19:224-247.
42. Yeatman JD, Dougherty RF, Myall NJ, Wandell BA, Feldman HM. Tract profiles of white matter properties: automating Fiber-tract quantification. *PLoS One.* 2012;7:e49790.
43. Garyfallidis E, Brett M, Amirbekian B, et al. Dipy, a library for the analysis of diffusion MRI data. *Front Neuroinform.* 2014;8.
44. Kruper J, Yeatman JD, Richie-Halford A, et al. Evaluating the reliability of human brain white matter tractometry. *Apert Neuro.* 2021;2021:25.
45. Tournier JD, Calamante F, Connelly A. Improved probabilistic streamlines tractography by 2nd order integration over fibre orientation distributions. *Proc Int Soc Mag Reson Med.* 2010;18:1670.
46. Jeurissen B, Tournier JD, Dhollander T, Connelly A, Sijbers J. Multi-tissue constrained spherical deconvolution for improved analysis of multi-shell diffusion MRI data. *Neuroimage.* 2014;103:411-426.
47. Tournier JD, Smith R, Raffelt D, et al. MRtrix3: a fast, flexible and open software framework for medical image processing and visualisation. *Neuroimage.* 2019;202:116137.
48. McKinnon ET, Jensen JH. Measuring intra-axonal T2 in white matter with direction-averaged diffusion MRI. *Magn Reson Med.* 2019;81:2985-2994.
49. Pizzolato M, Andersson M, Canales-Rodríguez EJ, Thiran JP, Dyrby TB. Axonal T2 estimation using the spherical variance of the strongly diffusion-weighted MRI signal. *Magn Reson Med.* 2022;86:118-134.
50. Varela-Mattatall G, Dubovan PI, Santini T, Gilbert KM, Menon RS, Baron CA. Single-shot spiral diffusion-weighted imaging at 7T using expanded encoding with compressed sensing. *Magn Reson Med.* 2023;90:615-623.
51. Wilm BJ, Nagy Z, Barmet C, et al. Diffusion MRI with concurrent magnetic field monitoring. *Magn Reson Med.* 2015;74:925-933.
52. Ma R, Akçakaya M, Moeller S, Auerbach E, Uğurbil K, Van De Moortele PF. A field-monitoring-based approach for correcting eddy-current-induced Artifacts of up to the 2nd spatial order in human-connectome-project-style multiband diffusion MRI experiment at 7T: a pilot study. *Neuroimage.* 2020;216:116861.
53. Ramos-Llordén G, Park DJ, Kirsch JE, et al. Eddy current-induced artifact correction in high B-value ex vivo human brain diffusion MRI with dynamic field monitoring. *Magn Reson Med.* 2024;91:541-557.
54. Feizollah S, Tardif CL. High-resolution diffusion-weighted imaging at 7 tesla: single-shot readout trajectories and their impact on signal-to-noise ratio. *Spatial Resol Accur NeuroImage.* 2023;274:120159.
55. Huang SY, Tian Q, Fan Q, et al. High-gradient diffusion MRI reveals distinct estimates of axon diameter index within different white matter tracts in the in vivo human brain. *Brain Struct Funct.* 2020;225:1277-1291.
56. Veraart J, Novikov DS, Christiaens D, Ades-aron B, Sijbers J, Fieremans E. Denoising of diffusion MRI using random matrix theory. *Neuroimage.* 2016;142:394-406.
57. Lakens D. Calculating and reporting effect sizes to facilitate cumulative science: a practical primer for t-tests and ANOVAs. *Front Psychol.* 2013;4:863.
58. Faul F, Erdfelder E, Buchner A, Lang AG. Statistical power analyses using G*power 3.1: tests for correlation and regression analyses. *Behav Res Methods.* 2009;41:1149-1160.
59. Vos SB, Tax CMW, Luijten PR, Ourselin S, Leemans A, Froeling M. The importance of correcting for signal drift in diffusion MRI. *Magn Reson Med.* 2017;77:285-299.
60. Fan Q, Eichner C, Afzali M, et al. Mapping the human connectome using diffusion MRI at 300 mT/m gradient strength: methodological advances and scientific impact. *Neuroimage.* 2022;254:118958.

SUPPORTING INFORMATION

Additional supporting information may be found in the online version of the article at the publisher's website.

Figure S1. Histograms of the MR axon radius (r_{MR}) distributions in white matter comparing test and retest measurements for all subjects. Mean (μ), median (M) and SD (σ) of the distributions are shown in the legend.

Figure S2. Histograms of the MR axon radius (r_{MR}) distributions in white matter comparing EPI and spiral data for all subjects and sessions. Mean (μ), median (M) and SD (σ) of the distributions are shown in the legend.

Figure S3. Histograms of the MR axon radius (r_{MR}) distributions in the corpus callosum comparing test and retest measurements for all subjects. Mean (μ), median (M), and SD (σ) of the distributions are shown in the legend.

Figure S4. Bland–Altman plots of all subjects for all white matter voxels. Solid lines represent the absolute mean difference and the limits of agreement, calculated as $1.96 \times \sigma$, where σ is the SD.

Figure S5. Left: Mean b -value across all subjects along the left CST from inferior to superior positions. Right: Corresponding mean axon radii along the left CST as shown in Figure 6 (top left and right) of the paper.

Figure S6. Histograms of difference (%) between test and retest of powder-averaged signals in the white matter. The difference Δ (%) was calculated for both shells as $\Delta = (\bar{S}_{\text{test}} - \bar{S}_{\text{retest}}) / \bar{S}_{\text{test}}$, where \bar{S} is the powder-averaged signal. Three different subjects with small, moderate and large bias of the MR axon radius are displayed.

Table S1. Ratio of the mean SNR measure across all subjects and sessions as in Figure 2 of the paper. The ratios are listed for the white matter (WM) mask used in the paper and a tighter white matter mask. For the tighter mask, a higher threshold of >0.98 and an additional binary erosion was used to make sure only pure white matter voxels were selected.

Table S2. Absolute distances of the center of the FOV to the scanner's isocenter for both measurements (Test

and Retest) and each subject (only spiral datasets). Also, the absolute distances between the centers of the FOV of both measurements, that is, the difference between the two scan positions are shown. In the last column the respective bias is shown, which is the mean of the differences between Test and Retest for all white matter voxels as in the Bland–Altman plots in Figure 7.

How to cite this article: Veldmann M, Edwards LJ, Pine KJ, et al. Improving MR axon radius estimation in human white matter using spiral acquisition and field monitoring. *Magn Reson Med.* 2024;1-15. doi: 10.1002/mrm.30180